J. Fluid Mech. (1985), *vol.* 155, *pp.* 37–57
Printed in Great Britain

Longitudinal vortices imbedded in turbulent boundary layers. Part 1. Single vortex

By I. M. M. A. SHABAKA†, R. D. MEHTA‡ AND P. BRADSHAW
Department of Aeronautics, Imperial College, London

(Received 26 November 1984)

Detailed mean-flow and turbulence measurements have been made in a low-speed turbulent boundary layer in zero pressure gradient with an isolated, artificially generated vortex imbedded in it. The vortex was generated by a half-delta wing on the floor of the wind-tunnel settling chamber, so that the vortex entering the working section had the same circulation as that originally generated, while axial-component velocity variations were very much reduced, relative to the local mean velocity, from values just behind the generator. The measurements show that the circulation around the vortex imbedded in the boundary layer is almost conserved, being reduced only by the spanwise-component surface shear stress. Therefore the region of flow affected by the vortex continues to grow downstream, its cross-sectional dimensions being roughly proportional to the local boundary-layer thickness. The behaviour of the various components of eddy viscosity, deduced from measured Reynolds stresses, and of the various triple products, suggests that the simple empirical correlations for these quantities used in present-day turbulence models are not likely to yield flow predictions which are accurate in detail.

1. Introduction

This paper is one of a series on complex turbulent flows (Bradshaw 1975; Kline, Cantwell & Lilley 1981, 1982) and the first of a group dealing with relatively weak longitudinal vortices imbedded in otherwise two-dimensional constant-pressure turbulent boundary layers. Parts 2 and 3, by Mehta & Bradshaw and Shibl & Bradshaw, which are in preparation, deal with pairs of imbedded vortices, the flow between the vortices (the 'common flow') being respectively away from, and towards, the solid surface. Work on stronger vortices is in progress.

Longitudinal vortices generated in, or merging with, boundary layers are found in many flows of practical importance. In almost all cases *except* that of a long, straight, non-circular duct the longitudinal vorticity is acquired by an essentially inviscid mechanism, namely the lateral deflection of a pre-existing shear layer ('skew-induced' secondary flow or 'secondary flow of Prandtl's first kind'), rather than by turbulent Reynolds-stress gradients ('stress-induced' secondary flow or 'secondary flow of the second kind'). This skewing of an existing vorticity vector, discussed by Squire & Winter (1951) and Hawthorne (1951), is responsible for most of the streamwise component of vorticity even in conventional three-dimensional (3D) boundary-layer flows, where it appears as 'vortex sheets' parallel to the surface, rather than as discrete vortices. If skewing starts well downstream of the boundary-

† Present address: Dept of Aero. Engng, Cairo University
‡ Present address: Dept. of Aero. and Astro., Stanford University, CA.

layer origin, the region in which streamwise vorticity is affected by viscous or turbulent stresses is often much thinner than the boundary layer as a whole; it is an internal layer next to the surface, created by the condition $W = 0$ at the surface and having longitudinal vorticity of the opposite sign to that induced by skewing. The complications of surface-flow patterns are attributable largely to this opposing vorticity, and do not necessarily represent the outer-flow behaviour. If the internal layer of opposing vorticity leaves the surface, for example at the line of separation upstream of an obstacle, skew-induced vorticity can merge with stress-induced vorticity from the internal layer. In the present flow, this effect is seen as the creation of a weak opposing vortex near the surface, to one side of the main vortex.

Longitudinal vortices in turbulent boundary layers belong to the class of 'slender' turbulent flows, in which velocity gradients in the y and z directions are much larger than longitudinal (x-wise) gradients. The simplifications to the equations of motion that can be made in slender flows are analogous to, but more restricted than, the thin-shear-layer approximations for flows in which both x-wise and z-wise (spanwise) gradients are small compared to y-wise gradients. There are two difficulties arising from the presence of large gradients in two directions: numerical methods are more complicated, even in laminar flow, because elliptic equations with significant convective terms must be solved for the flow in the cross-flow plane; and turbulence models developed for mildly three-dimensional flows with small gradients in the z-direction cannot necessarily be trusted in slender flows. Once formed, the angular momentum of a single longitudinal imbedded vortex is reduced only by the spanwise component of surface shear stress, which is usually very small and in any case affects only the internal layer mentioned above. Therefore, isolated vortices in boundary layers tend to persist for very long distances downstream, the ratio of vortex size to boundary-layer thickness remaining roughly constant because the turbulence diffuses both. Vortex *pairs* which are close enough to exchange angular momentum by mixing decay more rapidly. In either case prediction of the decay of secondary flow is a severe test of a turbulence model.

One of the commonest imbedded vortex flows is that due to the horseshoe vortex formed in front of an obstacle such as a wing/body (or blade/hub, or building/ground) junction, producing vortices in the streamwise corners above and below the wing. If the wing lift coefficient is high, the vortices may drift away from the corners: otherwise, the two merge at the trailing edge to form a vortex pair with the common flow between them directed towards the body surface, thus unhelpfully dumping low-speed fluid from the wing wake into the body boundary layer (Young 1977). In wind-tunnel contractions of non-circular cross-section, secondary flow generated by lateral pressure gradients induces a vortex pair on the centreline of each wall, with common flow away from the wall, leading to an unusually thick boundary layer near the centreline of each working-section wall (Mokhtari & Bradshaw 1983). In flows over slender bodies at incidence, a vortex pair, with the common flow towards the surface, is found on the lee side (Peake & Tobak 1980). As expected even from inviscid flow considerations, two vortices with the common flow towards a solid surface tend to move apart: one case of this is the generation of 'bilge vortices' near the bow of a ship, which trail downstream on either side of the ship's bottom, distorting the hull boundary layer so that the flow entering the propeller is highly complicated (Hoffmann 1976; Wieghardt 1983). In turbulent boundary layers over concave surfaces, an array of contra-rotating vortices is generated by centrifugal instability and can persist for long distances downstream of the end of the region of significant curvature (Smits, Young & Bradshaw 1979) even though – again – mixing of adjacent

vortices reduces their angular momentum. Hoffmann, Muck & Bradshaw (1985) concluded that the correspondence between curvature-induced and skew-induced vortices is not close enough to be helpful in development of calculation methods. Large arrays of contra-rotating 'roll vortices' are generated in many kinds of forced-convection buoyant flows, but are again likely to be significantly different in structure from skew-induced vortex pairs. A buoyancy-driven vortex *pair* with common flow upward was found by Haines & Smith (1983) above a streamwise line source of buoyancy simulating a forest fire: their flow appears not to have been fully turbulent, and detailed comparisons with skew-induced vortices would not be useful.

The object of the present series of papers on single and double imbedded vortices is to provide understanding and data for cases that are simple enough to be used in the development of turbulence models. According to the usual principles, models that satisfactorily predict the basic phenomena in simple flows should also predict these phenomena in more complicated flows. In the current uncertain state of turbulence modelling and numerical methods, it seems essential, initially, to investigate complex-flow phenomena one at a time in flows that are geometrically simple. In practical cases, imbedded longitudinal vortices are usually generated by lateral skewing of a pre-existing shear layer, and therefore develop in a wholly three-dimensional boundary layer, often in a significant pressure gradient and on a doubly curved surface. As a result, previous measurements on imbedded longitudinal vortex flows, such as those reviewed by Peake & Tobak, have mostly been made in configurations which are inconveniently complicated for use in the development of turbulence models. In fact, both manual and computerized searches of the literature have revealed no experiment on imbedded vortices in otherwise two-dimensional boundary layers, with the exception of the mean-flow measurements of Tanaka & Suzuki (1980). Further, few of the previous experiments on imbedded vortices in more complicated flows have included enough turbulence measurements to be directly useful in developing or testing turbulence models, mainly because of the difficulty of measuring the crossflow-plane shear stress, $\overline{vw}$. For a review of suitable test cases for secondary flow of the first kind see the evaluation report by Dean in Kline *et al.* (1981); the recommended cases were the curved-duct experiment of Humphrey, Whitelaw & Yee (1981) and the wing/body junction flow of Shabaka & Bradshaw (1981), in both of which the longitudinal vortices are imbedded in the region of interaction of the boundary layers on two perpendicular walls, which is complicated enough even in the absence of skew-induced vorticity. For a review of ship boundary-layer data and comparison with calculation see Larsson (1981); the vortex-dominated flow near the stern of a ship contains such strong longitudinal gradients that the boundary-layer approximation is not trustworthy and the effect of the turbulence model is difficult to estimate.

The present paper describes the interaction of a single, weak, artificially generated vortex and an otherwise two-dimensional turbulent boundary layer in nominally zero pressure gradient. This is the simplest possible vortex/boundary-layer interaction, but should be sufficiently general to be useful as a test case for calculation methods intended to predict general imbedded-vortex flows. (We are currently investigating flows with pressure gradient, and also stronger vortices in, or just outside, a boundary layer.) Although we have set up a flow that is very simple geometrically, the behaviour of turbulence quantities is rather complicated. In particular, we find that 'gradient diffusion' approximations for various turbulence quantities, which are acceptable, if not admirable, in many two-dimensional flows, are totally unsatisfactory in the present flow. Reynolds stresses can have the opposite sign to the corresponding

velocity gradients (negative eddy viscosity) and triple products representing the turbulent diffusion of Reynolds stresses can have the wrong sign to be explicable in terms of gradients of the diffused quantity.

In complex turbulent flows like the present one, simple explanations of the results can hardly be expected: the results are intended to guide the development of prediction methods, and the discussion therefore centres on the behaviour of the terms in the Reynolds-stress transport equations. Our own computational work will be reported separately; we do not pretend to offer improved turbulence models here, but merely comment that present-day models, in which the triple-product terms are represented either by gradient-diffusion formulae or by simple combinations of Reynolds stresses, are unlikely to be adequate for detailed predictions of imbedded-vortex flows.

2. Apparatus and techniques

The measurements were made in the boundary layer on the floor of a 762 × 127 mm (30 × 5 in.) boundary-layer wind tunnel (Bradshaw 1972) with a two-dimensional contraction from a 30 × 45 in. settling chamber. The tunnel speed was 30 m s^{-1}, and the free-stream turbulence level was about 0.1 %. The vortex generator is a half-delta wing of 114 mm (4.5 in.) semi-span and 68° leading-edge sweep, mounted at 12° incidence (strictly, yaw) on the floor of the settling chamber. When a vortex is convected through a contraction, the circulation Γ around a contour which encloses the vortex (but not the wall boundary layers) is nominally conserved, and so are total-pressure differences. As a result, the vortex entering the working section has a cross-sectional area reduced by a factor equal to the contraction-area ratio, while the ratio of total pressure variations to the local mean dynamic pressure is reduced by a factor equal to the square of the contraction ratio. Thus, the flow entering the working section is an almost pure vortex some distance above the floor boundary layer: figure 1 (*a*) shows that the velocity defect is small, both in the vortex core and in the peninsula of fluid that is the non-rolled-up part of the vortex-generator wake. There is necessarily a flux of lateral momentum due to the side-force on the vortex generator, $\rho U \Gamma s$ or $4\rho\Gamma^2/C_L AR$), where s is the semi-span. This leads to an opposing stress-induced vorticity in the contraction wall boundary layer, but in the present case the laminar boundary layer entering the working section is only about 3 mm thick and its detailed properties should not affect the flow in the working section. A new, turbulent, boundary layer grows from a 1 mm diameter trip wire at the start of the working section. The boundary layer still has a distributed crossflow imposed by the lateral flux of momentum, but the major features observed are due to the vortex as such. The circulation round the vortex at entry to the working section was about $1.84U_e$ mm: the ratio of Γ to $U_e\delta$ at $x = 2551$ mm was 0.054, implying secondary flow velocities of order $0.05U_e$; and the ratio of the vortex generator side-force to $U_e^2\delta^2$ at the same station was 0.02, equivalent to a nominal crossflow velocity W of $0.02U_e$ over a cross-sectional area of δ^2 (say, the actual area of crossflow is likely to be several times larger and W therefore smaller).

Measurements were taken at one station before, and several stations after, the vortex entered the boundary layer. The measurements were made with conventional Pitot tubes (flow angles are less than 5°) and constant-temperature hot-wire anemometers. Cross-wire probes are relatively unaffected by transverse gradients, unlike pressure-probe yawmeters, and their inaccuracy is attributable mainly to random drift in calibrations, due to dust accretion and air-temperature variation. In

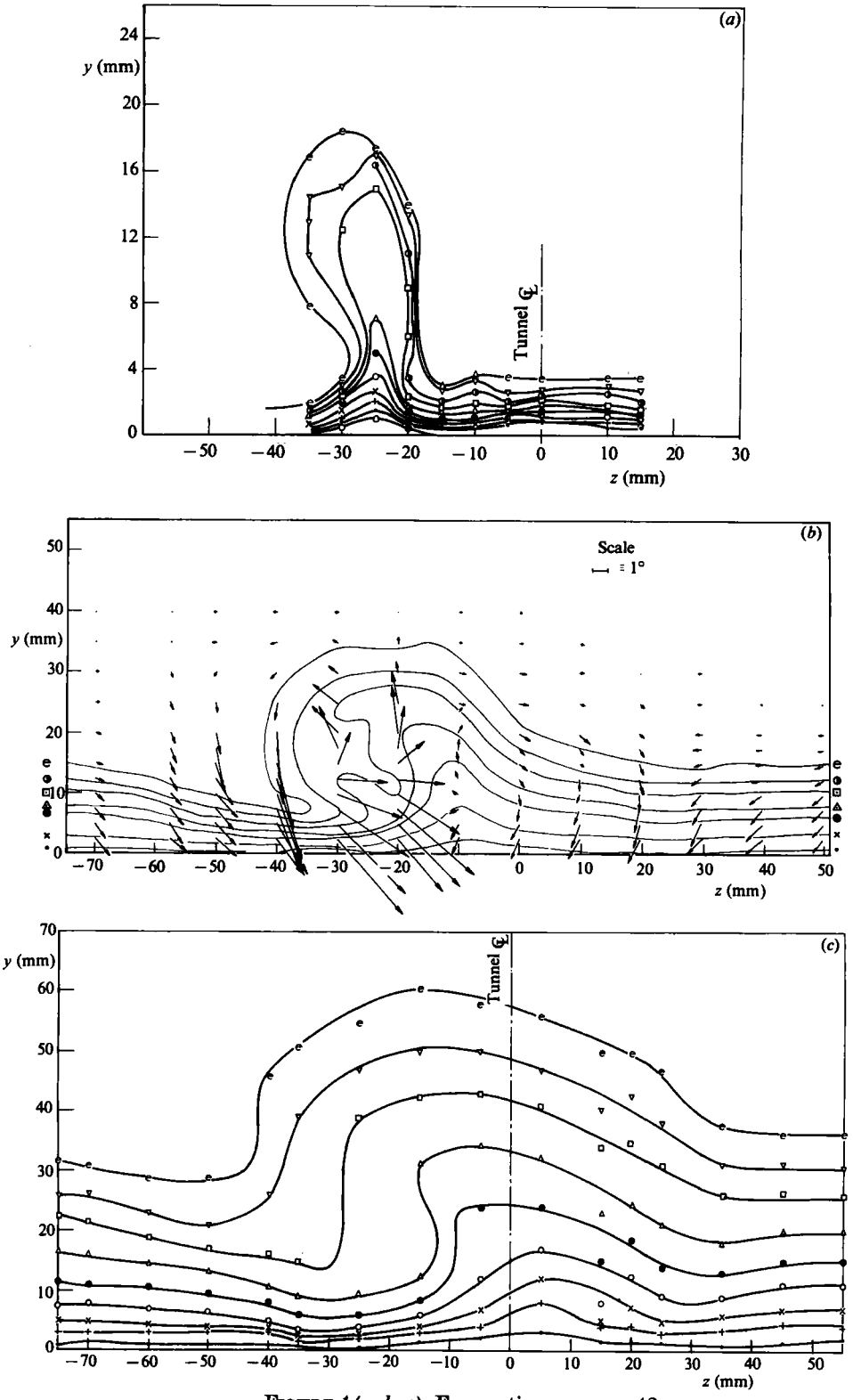

FIGURE 1 (*a*, *b*, *c*). For caption see page 42.

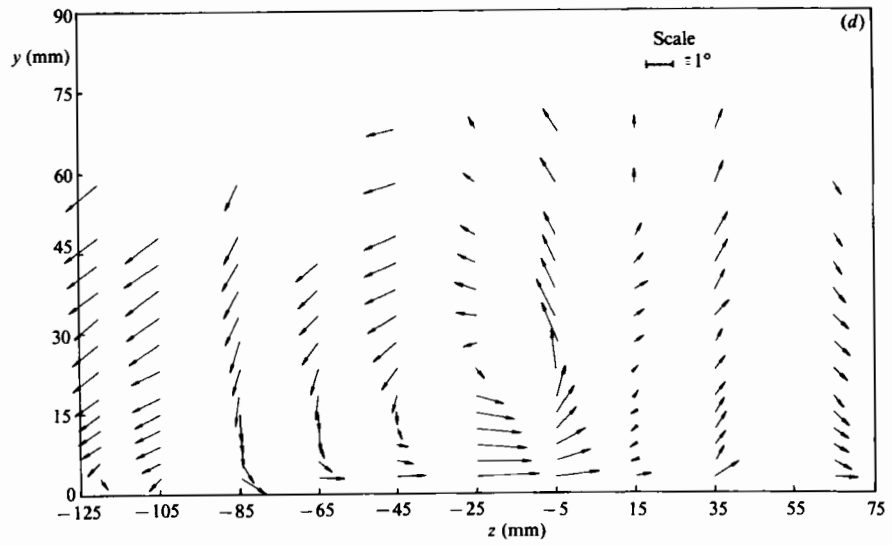

FIGURE 1. Mean velocity. (*a*) $x = 112$ mm (boundary layer not tripped). Contours of U/U_e: ○, 0.5; ., 0.6; +, 0.7; ×, 0.75; ○, 0.8; ●, 0.85; △, 0.90; □, 0.95; ◑, 0.975; ▽, 0.99; e, 0.995. (*b*) $x = 722$ mm. Streamwise-velocity contours and secondary-flow vectors: symbols as in figure 1 (*a*); arrow length proportional to secondary-flow angle, $(V^2+W^2)^{\frac{1}{2}}/U$. (*c*) $x = 2551$ mm: streamwise-velocity contours; symbols as in figure 1 (*a*). (*d*) $x = 2551$ mm: secondary-flow vectors (from hot-wire measurements with drift correction).

the final secondary-flow velocities derived from the hot-wire results an allowance for drift has been made, by requiring the measured V-component velocities to tend to zero at the surface.

Statistics involving both v and w component fluctuations were deduced from measurements with the plane of the probe's cross wires set successively at $+45°$ and $-45°$ to the (x, z)-plane, so that the differences between the wire signals were nominally $(v+w)/\sqrt{2}$ and $(v-w)/\sqrt{2}$ respectively. For temperature-conditioned sampling measurements, a spiral of electrical heating wire was placed just behind the vortex generator, so that the main part of the vortex passes inside the spiral and was (eventually) heated without appreciable loss of angular momentum. Temperature fluctuations were measured by a fast-response resistance thermometer (cold wire), using 1 μm platinum wire and driven by a conventional constant-current anemometer circuit. Fluctuating signals were recorded on analog magnetic tape, with a bandwidth of 20 kHz, and then transferred to digital tape for processing on a CDC 6500 computer. The general accuracy is shown by the smoothness with which the results asymptote, at large spanwise distances from the vortex, to those typical of two-dimensional boundary layers: see for example the eddy viscosity in figure 5 (*d*). The measurement grid was chosen as a compromise between the need to produce enough points for smooth curves and the need to minimize the time taken to survey the flow.

3. Results

This paper presents only a small selection of the results obtained. Full sets of first-, second- and third-order mean products of fluctuations at $x = 722$ and 2551 mm, and some derived quantities, are given by Bradshaw, Shabaka & Mehta (1982). Full data tabulations are available on magnetic tape.

Mean-velocity measurements are shown in figure 1. The vortex generator was offset so that the vortex entered the working section fairly near the tunnel centreline at $z = 0$, simply for convenience. In all cases the velocity near the wall appeared to obey the universal logarithmic profile (agreement in velocity is forced by the use of Preston tubes to measure skin friction, but agreement in velocity *gradient* is meaningful). Note that the measurements in figure 1 (*a*) were taken to define the initial behaviour of the vortex, with the tunnel-floor boundary layer untripped: the data near the wall are therefore not exactly consistent with the main results at stations further downstream. Figures 1 (*b*) and (*c*) show velocity contours at the main streamwise stations, with secondary-flow velocity components in vector form (figure 1 *d* shows the secondary velocity at $x = 2551$ mm). Longitudinal vorticity contours are shown in figure 2. The vorticity contours are clearly not very accurate, although the secondary-flow velocity pattern from which they were deduced is smooth enough (and much more informative to the reader): vorticity contours are included for use in checking predictions. The internal (surface) layer with the opposite sign of vorticity (positive $\partial W/\partial y$) was too thin to detect, but there is some evidence of a vortex of opposite sign on the positive-z side of the main vortex, where the internal layer is convected away from the surface by the circulation around the main vortex.

Figure 3 shows the skin-friction coefficient, deduced from Preston-tube measurements. Comparison with the secondary-flow vectors explains why there are two peaks in skin friction. We expect skin friction to be high at or near places where the V-component velocity near the surface is negative, bringing high-speed fluid down from above, and low when the flow is away from the surface. As well as the expected negative V on the downgoing side of the vortex, there is a downflow beyond the upgoing side, which indeed helps to supply the upflow. The engineering use of vortex generators to delay separation does, of course, rely on an overall increase in skin friction. Figure 3 shows that the spanwise drift of the pattern with increasing x, due to the lift on the vortex generator, is fairly small: skin friction was not measured at $x = 112$ mm but the minimum must have been near $z = -25$ mm, where the velocity contours in figure 1 (*a*) are furthest from the surface.

Detailed hot-wire measurements were made at two stations, $x = 722$ mm (not shown because of space limitations) and 2551 mm: the general trends are the same at both stations. Contour plots of all six independent Reynolds stresses are shown in figure 4. The primary shear stress $-\rho\overline{uv}$ is negative near $y = 25$ mm, $z = -25$ mm. The contours of the secondary shear stresses $\overline{uw}$ and $\overline{vw}$ (plotted as $\overline{u_i u_j}$ rather than its negative) are more complicated, because both stresses are zero far from the vortex and change sign within the vortex. The vortex is diffusing into the surrounding fluid and reducing its U-component momentum, so that $\overline{uw}$ should be negative on the positive-z side of the vortex and positive on the negative-z side, as is broadly the case. Longitudinal vorticity also diffuses, suggesting that $\overline{vw}$ should be positive on the positive-z side of the vortex and negative on the negative-z side, as is again the case. Rotation of the stressed fluid modifies the behaviour deduced from the above 'momentum' considerations: for instance, the negative $\overline{uv}$ values on the negative-z side of the vortex probably arise by anti-clockwise rotation of eddies carrying positive $\overline{uw}$.

Correlation coefficients, and eddy viscosities for $\overline{uv}$ and $\overline{uw}$, are shown in figure 5. The eddy viscosities have been normalized by $u_\tau\,\delta$, where δ is the local boundary-layer thickness to the point where $U = 0.995U_e$, for ease of comparison with the popular data fit in the outer layer of conventional boundary layers $\nu_t = 0.0168U_e\,\delta^* = 0.063u_\tau\,\delta$. Conventional values of R_{uv} (figure 5*a*) are attained near the surface at almost all

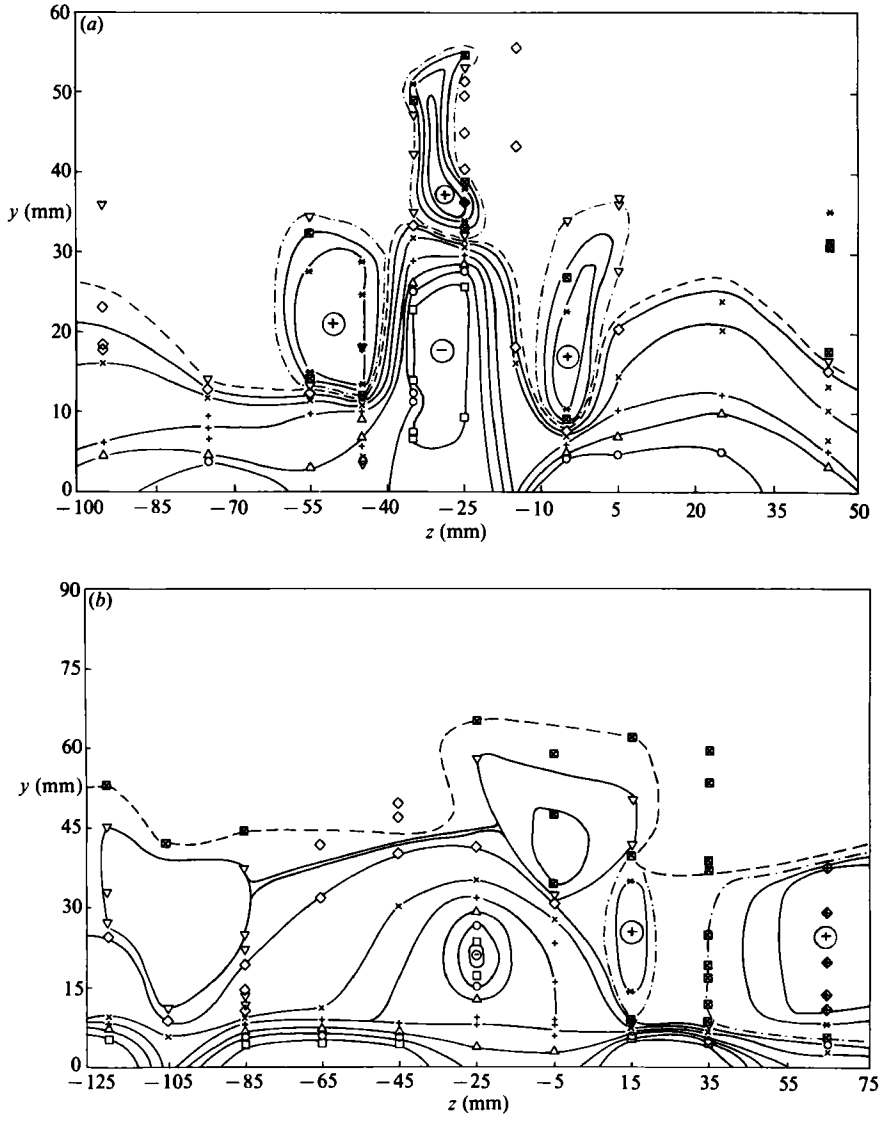

FIGURE 2. Longitudinal-vorticity contours: predominant vorticity is negative in these axes. In this and following figures, chain lines and dotted lines are 0+ and 0− contours respectively, and large circles indicate signs of surrounding regions but are not at exact extremum points. (*a*) $x = 722$ mm. ξ/U_e, m^{-1}: □, −6; ○, −4; △, −3; +, −2; ×, −1; ◇, −0.5; ▽, 0; ⊠, 0.5; *, 1.0; ⊕, 2.0. (*b*) $x = 2551$ mm. ξ/U_e, m^{-1}: □, −3; ○, −2.5; △, −2; +, −1.5; ×, −1; ◇, −0.5; ▽, −0.25; ⊠, 0; *, 0.5; ⊕, 1.5.

values of z, and quite large (negative) values are also attained near the top of the vortex, at say $z = -5$ to -45 mm, but elsewhere the turbulence structure is obviously grossly disturbed by the vortex, and R_{uv} of course changes sign in the region of positive $\overline{uv}$, shaded in figure 4(*d*). The contours of shear-stress structure parameter in figure 5(*b*) contain much the same information as the R_{uv} profiles but are easier to view: negative values occur all along the edge but, except near the downgoing side of the vortex, the corresponding shear stress is very small and within the likely experimental error. The variation of the eddy viscosities in figures 5(*c*) and (*d*) is

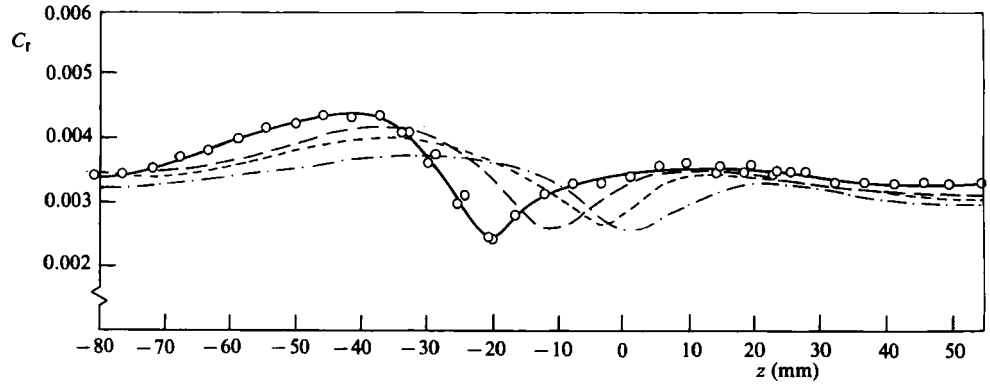

FIGURE 3. Skin-friction coefficient. Values of x, mm: ——, 722; ——, 1331; – – –, 1941; –·–, 2551. Data points for $x = 722$ mm only.

somewhat complicated, but at large positive or negative z the eddy viscosity for the primary shear stress $-\overline{uv}$ has nearly returned to the conventional boundary-layer value quoted above. The secondary eddy viscosity in figure 5(*d*) tends to 0/0 at large positive or negative z, as well as at large y: here and elsewhere, '0/0' behaviour gives a poor impression of the experimental accuracy.

Figures 6 and 7 show selected triple products and derived results, to be discussed below. Quantities like $\overline{uv^2}/\overline{uv}$ represent transport velocities of turbulence quantities, in this case the v-component transport velocity of $\overline{uv}$. Triple products are usually represented in calculation methods by eddy-diffusivity formulae, but our results suggest that the transport velocities are generally rather better behaved, and therefore simpler to correlate empirically. Diffusivities become infinite when the Reynolds-stress gradient is zero, unless the triple product is zero simultaneously: however, the transport velocities become infinite only where the transported quantity itself changes sign, which is rare for shear stress and impossible for normal stress or turbulent energy. In figure 7 the singularities are disguised by the contour-plotting process, but in any case figure 7 is intended as a warning rather than a presentation of quantitatively useful results.

An attempt was made to measure the intermittency factor in the vortex by heating it just downstream of the vortex generator, and declaring the flow to be turbulent when the instantaneous temperature rose above a pre-set threshold, and non-turbulent otherwise. Small temperature differences appear naturally in the boundary layer, because the air is heated by the blower driving the wind tunnel: thus, results outside the range shown in figure 8 are not to be trusted. However, the intermittency clearly falls off rapidly on either side of the vortex, showing that lateral 'snaking' of the vortex, induced by wind-tunnel turbulence or otherwise, is small. (These results were taken at one of the intermediate stations but should be typical of any value of x.)

4. Discussion

The selected results presented above contain no major surprises – that is, features likely to cause gross discrepancies in calculations by existing methods – but there are many minor complexities which, in sum, suggest that calculations by existing methods will not be accurate in detail. A similar conclusion for the corner-vortex flows mentioned above was reached at the 1981 Stanford Conference (Kline *et al.* 1982).

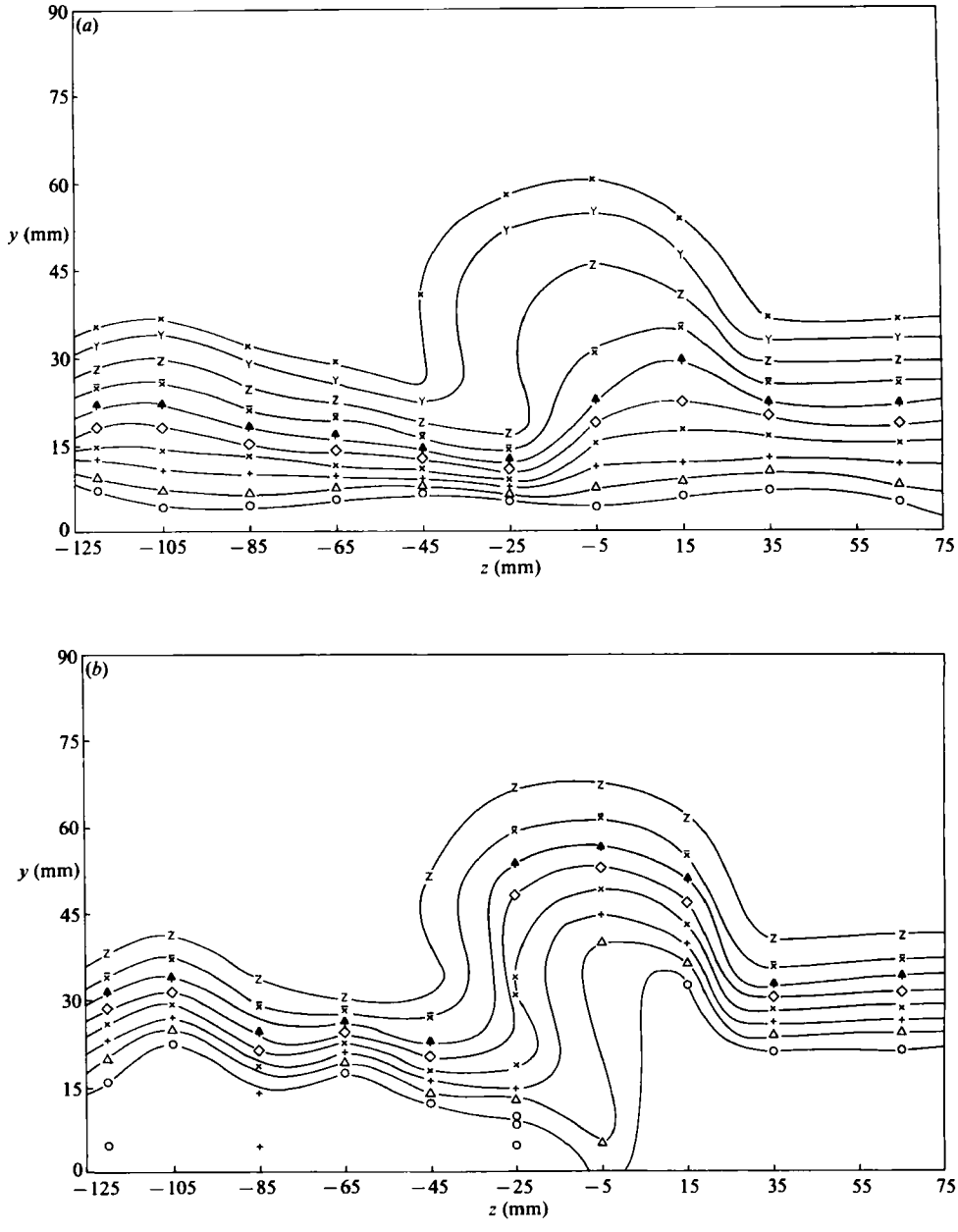

FIGURE 4(*a*, *b*). For caption see page 48.

The eddy diffusivities of Reynolds stress are ill-behaved for a fairly large region on either side of the vortex core, and significant negative values appear in regions in which the shear stress, although small, is not so small as to be unimportant. The only way in which an 'algebraic' eddy-viscosity calculation method (that is, one in which the eddy viscosity is directly related to local mean-flow integral parameters) could be made to work for imbedded vortex flows is by directly relating the eddy viscosity to the y, z coordinates within the vortex; such relations would probably not serve

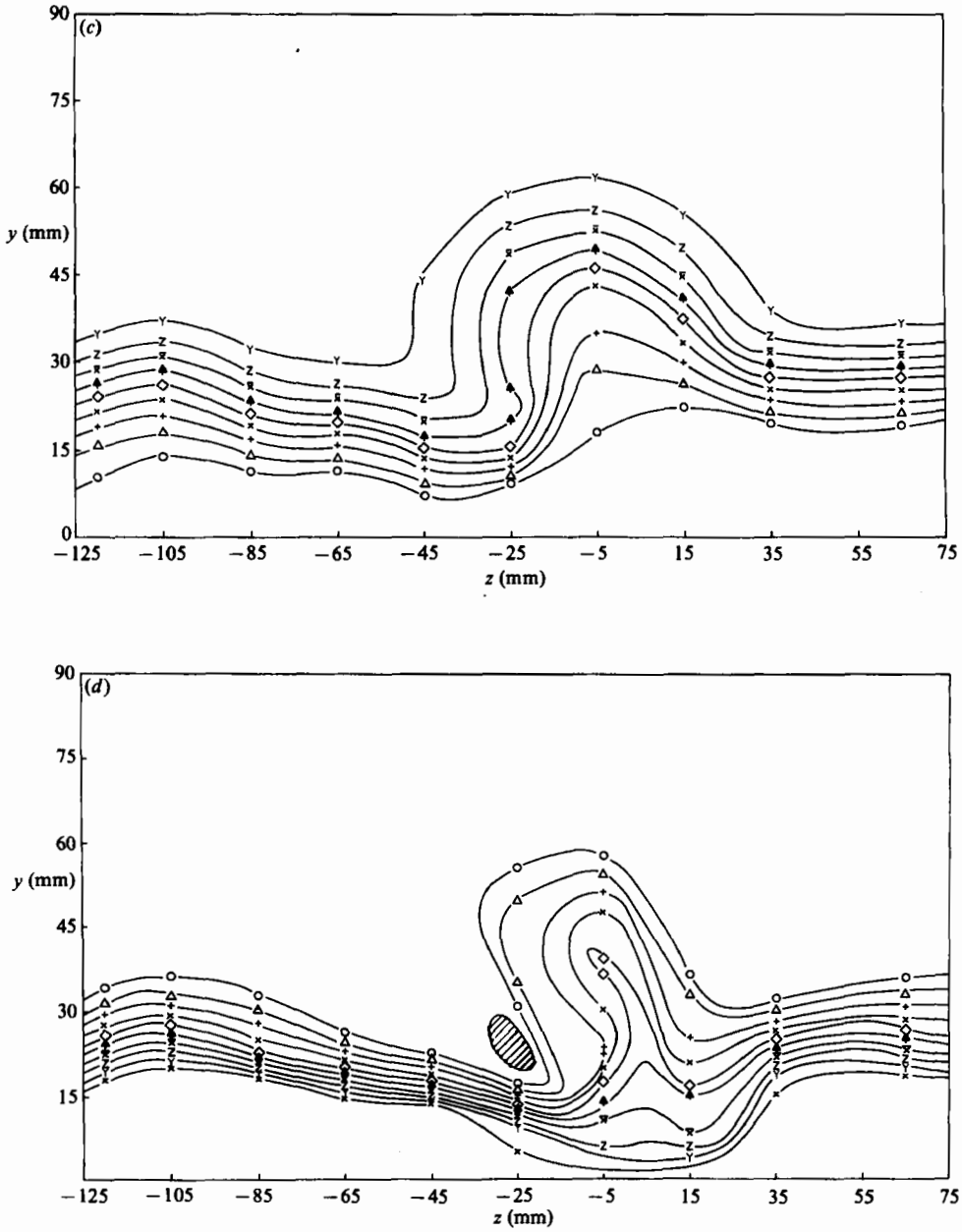

FIGURE 4(*c*, *d*). For caption see page 48.

for vortices with added complications such as longitudinal pressure gradient. A more sophisticated alternative is to use calculation methods based on term-by-term modelling of the Reynolds-stress transport equations, but one is then faced with the difficulty of modelling, by eddy diffusivity or otherwise, the triple products of velocity fluctuations, and also the pressure–strain redistribution term. The secondary-flow velocities measured in the present experiment are not sufficiently accurate for reliable estimates of the mean transport (convection) terms to be derived, and the same is

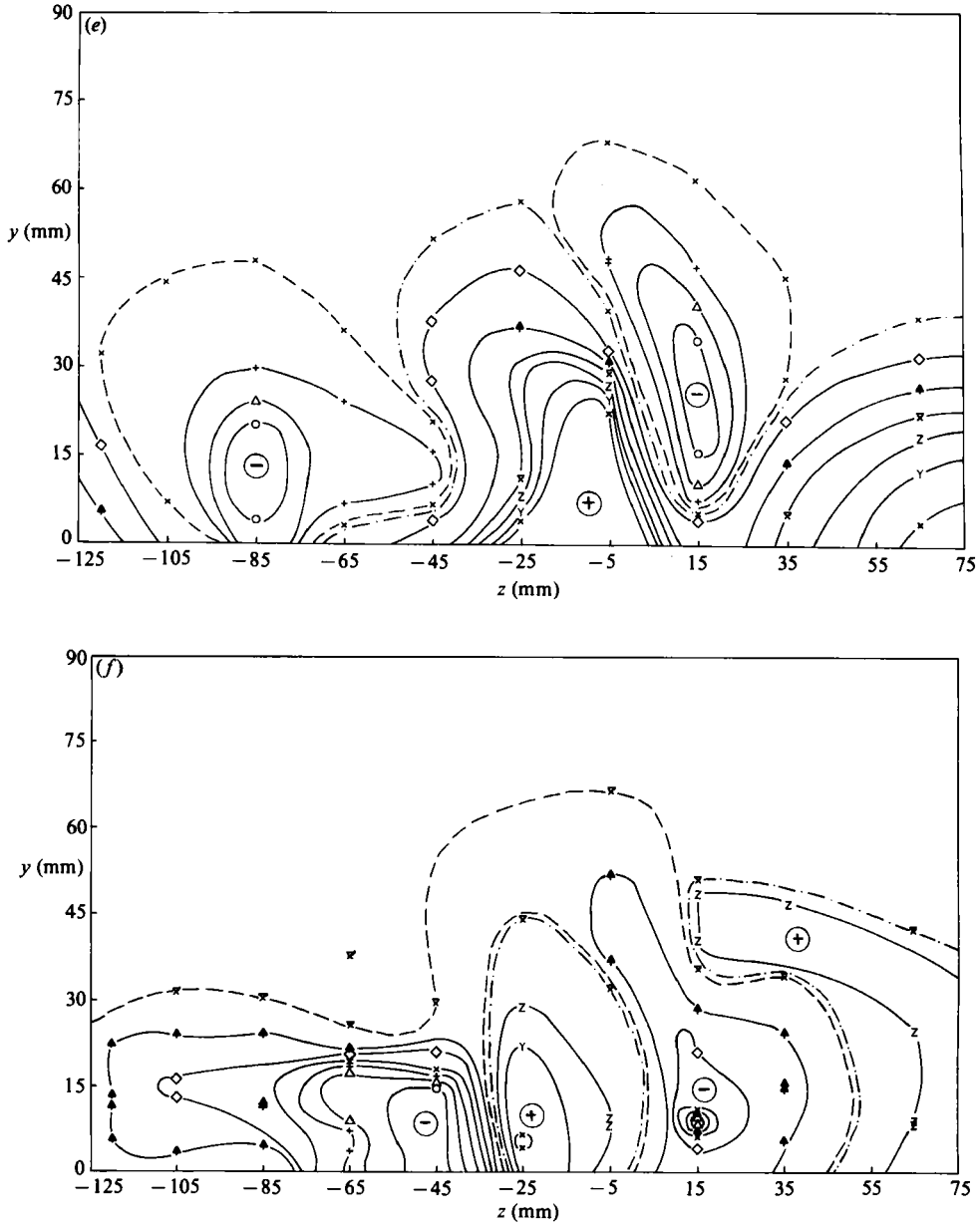

FIGURE 4. Contours of $\overline{u_i u_j}/U_e^2$, $x = 2551$ mm. (*a*) $\overline{u^2}$: ⊠, 0.0005; Y, 0.001; Z, 0.002; ⧖, 0.003; ♠, 0.004; ◇, 0.005; ×, 0.006; +, 0.007; △, 0.008; ○, 0.009. (*b*) $\overline{v^2}$: Z, 0.0002; ⧖, 0.0004; ♠, 0.0006; ◇, 0.0008; ×, 0.001; +, 0.0012; △, 0.0014; ○, 0.0016. (*c*) $\overline{w^2}$: Y, 0.0003; Z, 0.0006; ⧖, 0.0009; ♠, 0.0012; ◇, 0.0015; ×, 0.0018; +, 0.0021; △, 0.0024; ○, 0.0027. (*d*) $-\overline{uv}$: ○, 0.0001; △, 0.0002; +, 0.0003; ×, 0.0004; ◇, 0.0005; ♠, 0.0006; ⧖, 0.0007; Z, 0.0008; Y, 0.0009; ■, 0.0010. Hatching denotes $\overline{uv} > 0$. (*e*), $\overline{uw}$: ○, −0.0006; △, −0.0004; +, −0.0002; ×, 0; ◇, 0.0002; ♠, 0.0004; ⧖, 0.0006; Z, 0.0008; Y, 0.0010; ■, 0.0012. (*f*) $\overline{vw}$: ○, −0.0006; △, −0.0005; +, −0.0004; ×, −0.0003; ◇, −0.0002; ♠, −0.0001; ⧖, 0; Z, 0.0001; Y, 0.0002; ■, 0.0003.

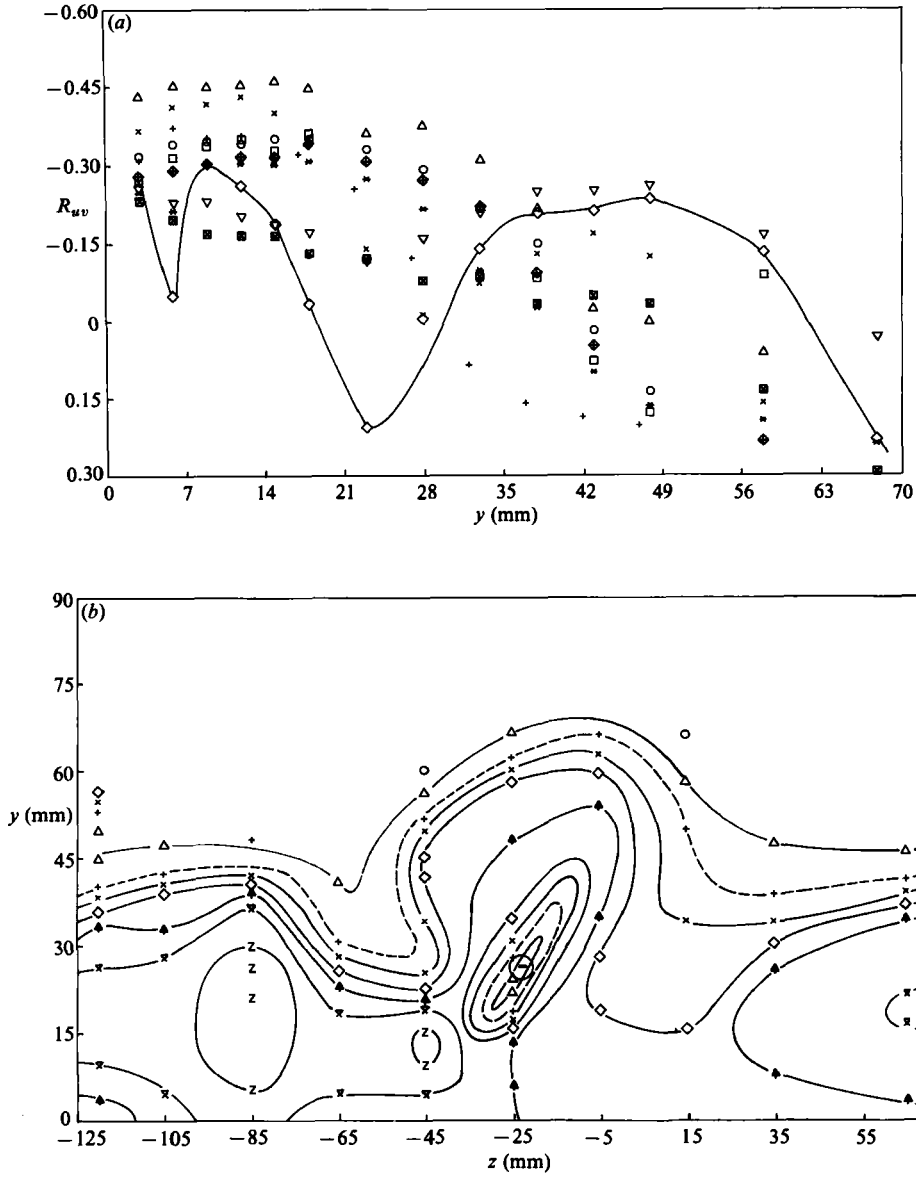

FIGURE 5(*a*, *b*). For caption see page 50.

probably true of most other experiments on secondary flows. We have therefore not attempted to evaluate the terms in the Reynolds-stress transport equations so as to obtain the pressure-strain term by difference. The present results should, however, be directly useful for modelling the triple-product terms, and of course provide a detailed test case for Reynolds-stress prediction: calculations could be started at $x = 722$ mm and continued until $x = 2551$ mm. The longitudinal pressure gradient can be assumed to be negligible: we did not attempt to measure static pressure within the fluid, since the effect of turbulence on the static pressure tube would have been as large as the expected pressure changes, but, if the cross-sectional velocity

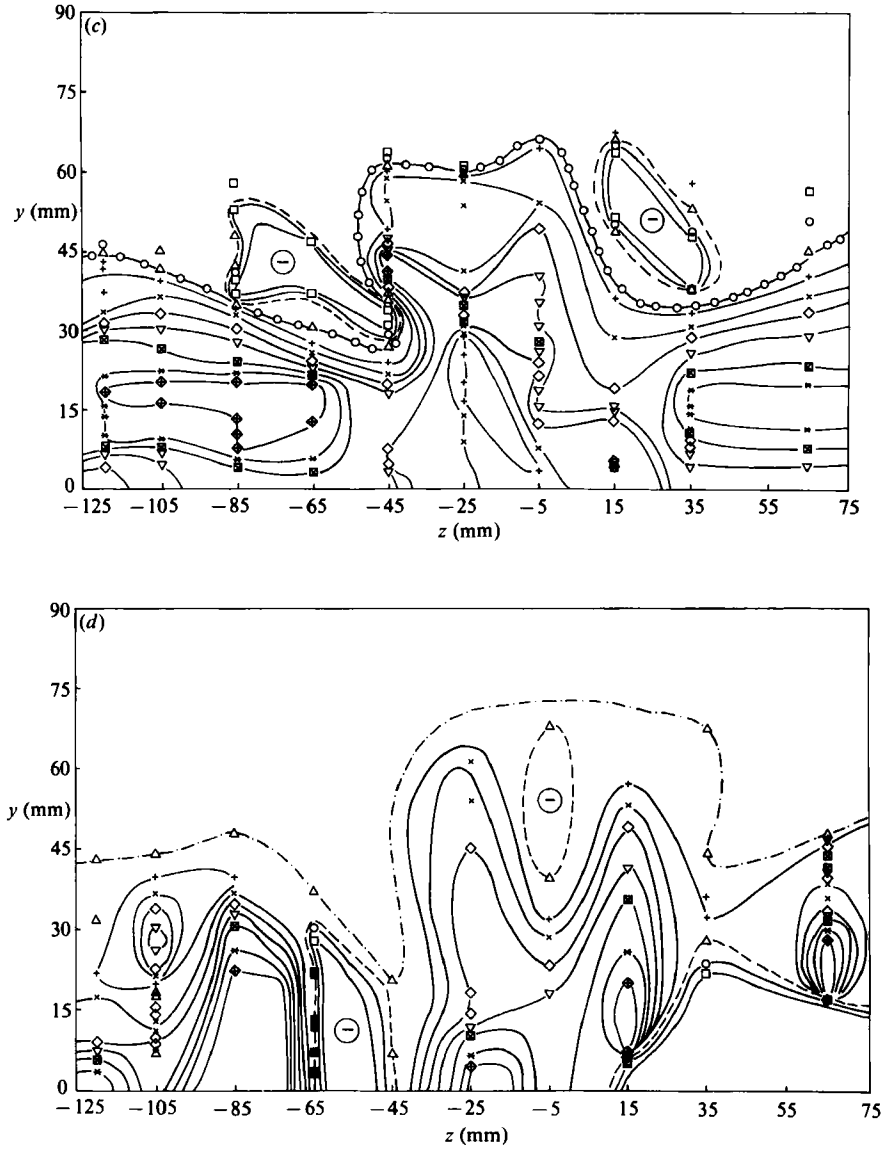

FIGURE 5. Shear-stress parameters, $x = 2551$ mm. (*a*) Profiles of R_{uv}: □, $z = -120$ mm; ○, -105; △, -85; +, -65; ×, -45; ◇, -25; ▽, -5; ⊠, $+15$; *, 35; ⊕, 65. (*b*) Contours of $a_1 = -\overline{uv}/(\overline{u^2}+\overline{v^2}+\overline{w^2})$: ○, -0.10; △, -0.05; +, 0; ×, 0.025; ◇, 0.05; ♠, 0.075; ⧖, 0.10; Z, 0.125. (*c*) Contours of eddy viscosity for primary shear stress, $[-\overline{uv}/(\partial U/\partial y)]/(u_\tau \delta)$: □, -0.02; ○, -0.01; △, 0; +, 0.01; ×, 0.02; ◇, 0.03; ▽, 0.04; ⊠, 0.05; *, 0.06; ⊕, 0.07. (*d*) Contours of eddy viscosity for (x, z)-plane shear stress, $-\overline{uw}/(\partial U/\partial z)/(u_\tau \delta)$: □, -0.1; ○, -0.05; △, 0; +, 0.02; ×, 0.04; ◇, 0.06; ▽, 0.08; ⊠, 0.10; *, 0.15; ⊕, 0.20.

distribution is fully specified in the initial conditions for a calculation method, the cross-sectional pressure distribution need not be prescribed as well, since it can in principle be derived from integration of the Poisson equation for pressure, given the pressure at infinity.

The secondary-flow vectors in (say) figure 1 (*d*) differ interestingly from those

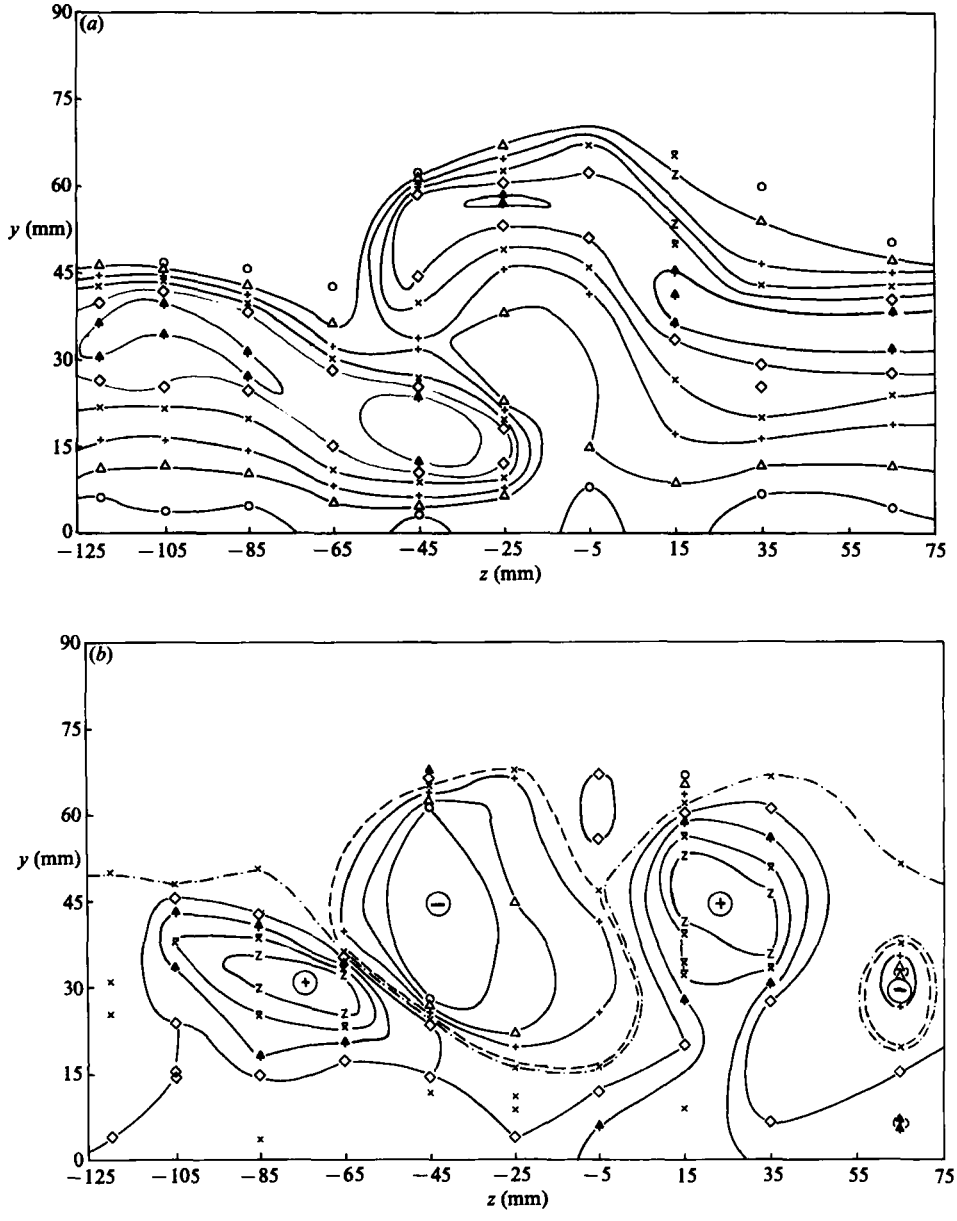

FIGURE 6(*a*, *b*). For caption see page 52.

reported by Shabaka & Bradshaw (1981) for the flow due to a single vortex in a wing–body junction. There, the maximum longitudinal vorticity was found fairly close to the surface, where it necessarily resided mainly in $\partial W/\partial y$ because $\partial V/\partial z$ is forced to be small near a solid surface, $y = 0$, where $V = 0$: however, this does not automatically imply that the *total* vorticity shall be unusually large near $y = 0$. Obviously, the regions of large longitudinal vorticity near the surface on either side of the vortex core in the present flow are also due predominantly to (negative) $\partial W/\partial y$: there must be a region of positive $\partial W/\partial y$ very close to the surface to satisfy the no-slip

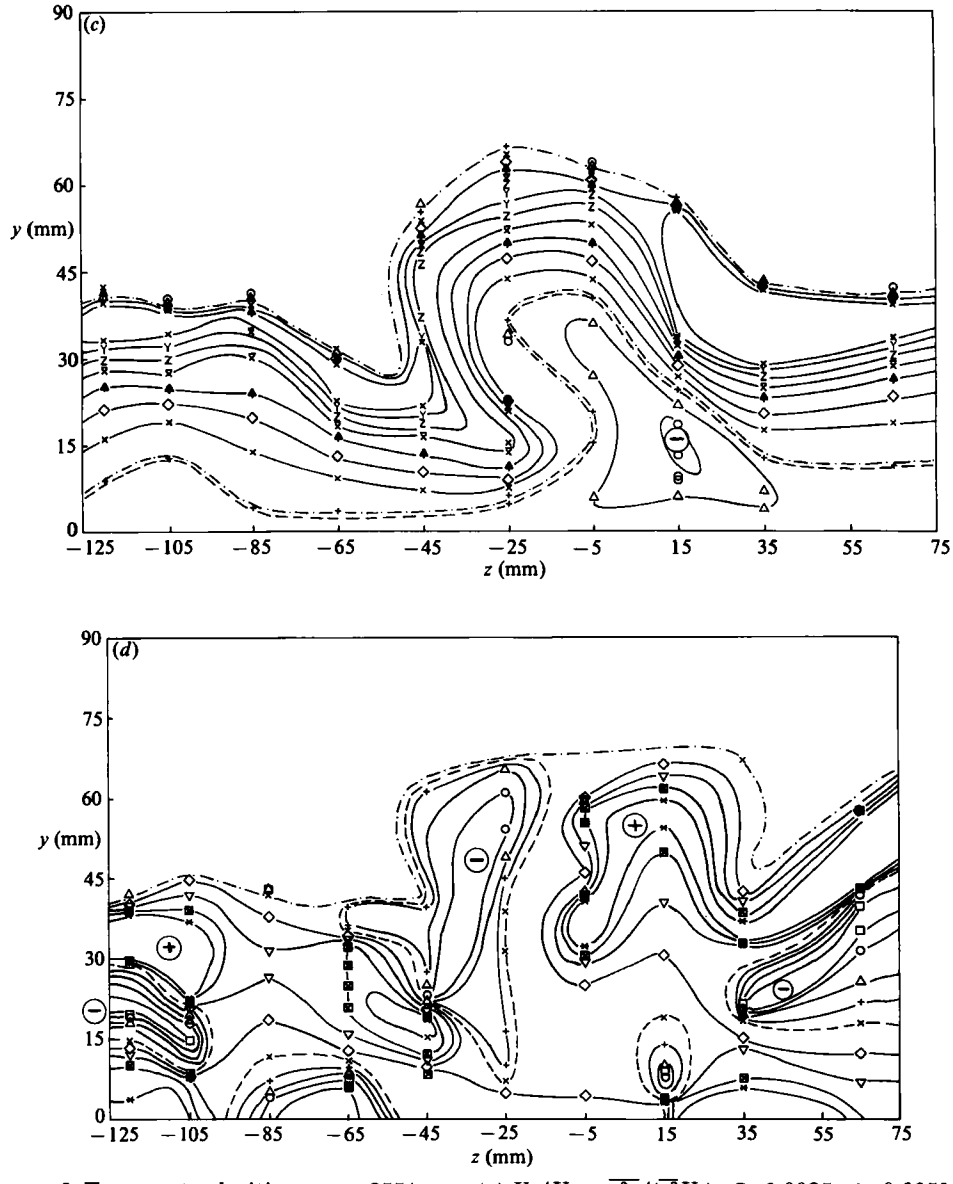

FIGURE 6. Transport velocities at $x = 2551$ mm. (*a*) $V_q/U_e = \overline{q^2v}/(\overline{q^2}U_e)$: ○, 0.0025; △, 0.0050; +, 0.0075; ×, 0.010; ◇, 0.0125; ♦, 0.0150; (☒, 0.0175; Z, 0.020; implausible 0/0 values at $z = 15$ mm). (*b*) $W_q/U_e = \overline{q^2w}/(\overline{q^2}U_e)$: ○, −0.0075; △, −0.0050; +, −0.0025; ×, 0; ◇, 0.0025; ♦, 0.0050; ☒, 0.0075; Z, 0.010. (*c*) $V_{uv}/U_e = \overline{uv^2}/(\overline{uv}U_e)$: ○, −0.02; △, −0.01; +, 0; ×, 0.01; ◇, 0.02; ♦, 0.03; ☒, 0.04; Z, 0.05; Y, 0.06; ■, 0.07. (*d*) $W_{uw}/U_e = \overline{uw^2}/(\overline{uw}U_e)$: □, −0.1; ○, −0.075; △, −0.050; +, −0.025; ×, 0; ◇, 0.025; ▽, 0.050; ⊠, 0.075; *, 0.1.

condition. The three regions with a high vorticity of opposite sign to that of the main vortex, seen surrounding the main vortex at $x = 722$ mm (figure 2*a*) are barely noticeable at $x = 2551$ mm (figure 2*b*). In the latter figure the counter-circulation region near $z = 60$ mm arises from the change of sign in V between $z = 35$ mm and 65 mm (figure 1*d*), and may possibly be unreal: the distortion of the streamwise

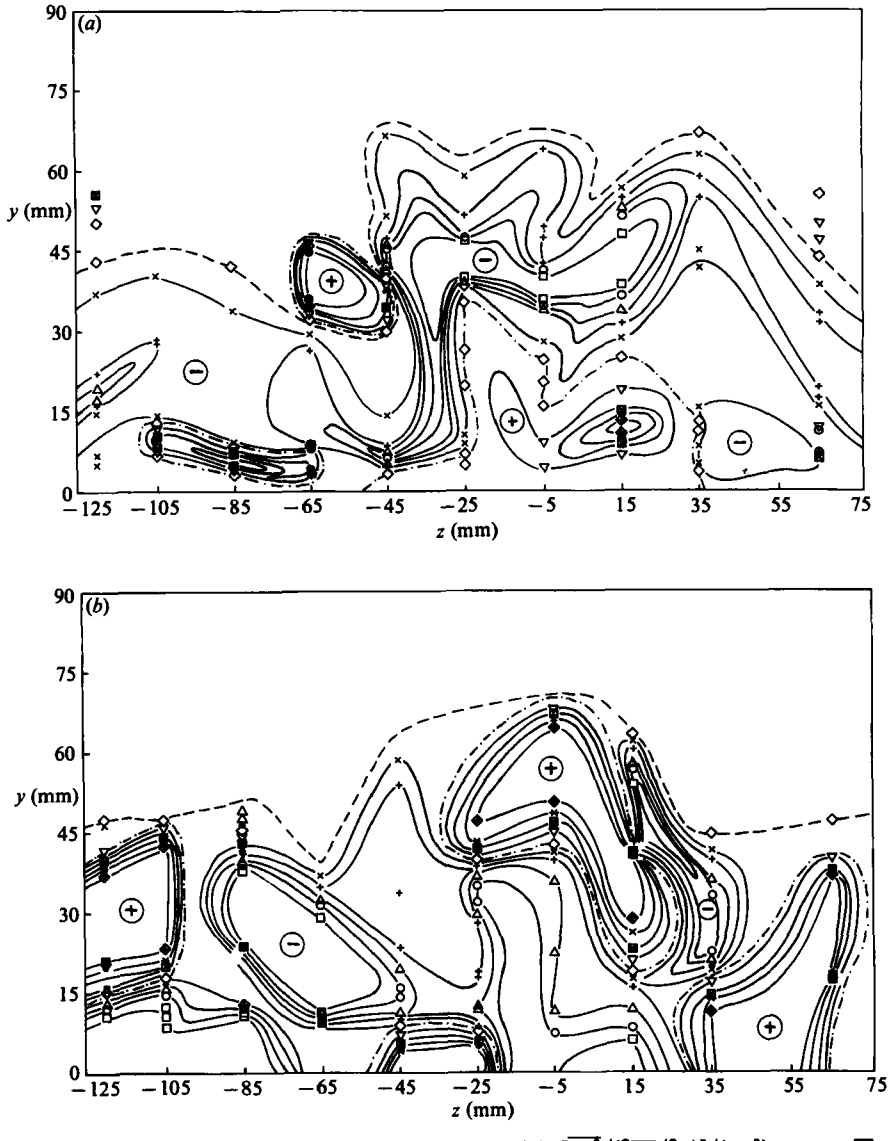

FIGURE 7. Eddy-diffusivity contours, $x = 2551$ mm. (*a*) $[\overline{uv}^2/(\partial\overline{uv}/\partial y)]/(u_\tau\delta)$, mm: □, −0.6; ○, −0.4; △, −0.3; +, −0.2; ×, −0.1; ◇, 0; ▽, 0.1; ⊠, 0.2; *, 0.3; ⊕, 0.4; ⊕, 0.5. (*b*) $[\overline{uw}^2/(\partial\overline{uw}/\partial z)]/(u_\tau\delta)$, mm: □, −0.5; ○, −0.3; △, −0.2; +, −0.1; ×, −0.05; ◇, 0; ▽, 0.1; ⊠, 0.2; *, 0.3; ⊕, 0.5.

velocity contours in figure 1(*c*) suggests a counter-vortex near the surface at $z = 25$ mm approximately.

The Reynolds-normal-stress contours are qualitatively explicable as distortion of the boundary-layer turbulence by a superimposed vortex. However, the region of negative shear stress (positive $\overline{uv}$) near $z = -25$ mm in figure 4(*d*) is of some interest. As mentioned above, it can be 'explained' by the rotation about the x axis of eddies bearing positive $\overline{uw}$ (figure 4*e*). In Part 3 we will show that $\overline{uv}$ is almost zero in the cores of a vortex pair with the 'common flow' between them towards the surface: the present phenomenon provides a first hint of this. The shear stress in the xz plane,

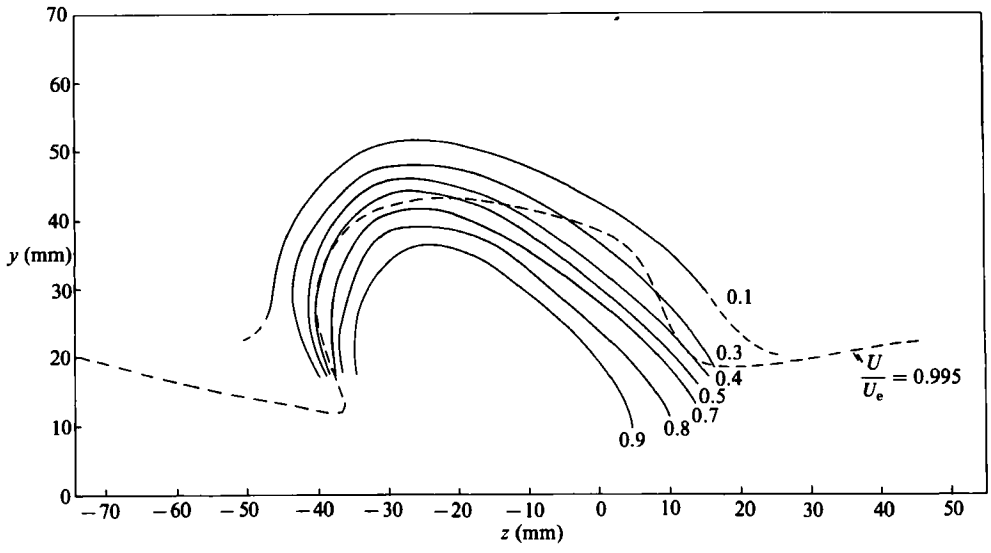

FIGURE 8. Temperature-intermittency contours at $x = 1331$ mm.

$-\overline{uw}$, is almost as large as $-\rho\overline{uv}$, but its distribution is very different. The main positive and negative regions near the vortex core are of the sign expected from the z-wise diffusion of x-component momentum, while the regions of uw at larger positive or negative z (visible at both x stations although the details are different) are of the sign expected from eddy-viscosity arguments based on the sign of $\partial W/\partial y$. The yz-plane shear stress $\overline{vw}$ is notoriously difficult to measure with accuracy, but in view of the streamwise trends in other quantities the detailed differences in $\overline{vw}$ distributions between $x = 722$ mm (not shown here) and $x = 2551$ mm (figure 4*f*) seem to be generally real. Both show a region of strongly positive $\overline{vw}$ on the positive-z side of the vortex, where $\partial W/\partial y$ is strongly negative, but apart from this the relation of $\overline{vw}$ to $\partial W/\partial y$ or $\partial V/\partial z$ is not simple.

The shear correlation coefficients and stress-energy ratio (figure 5) are more use than the raw Reynolds stresses for identifying structural changes. Only R_{uv} is shown here, but all three shear-stress correlation coefficients reach extreme values of ± 0.4 or more, although the measurements of R_{vw} are somewhat scattered. Large values of R_{uw} might be explained in terms of the 'rotation of primary shear stress' argument used above, but the large values of R_{vw} cannot be explained in this way. The vortex motion does far more than simply distort the pre-existing Reynolds stress pattern.

Our extensive triple-product measurements are represented in this paper only by some derived results for eddy diffusivities and transport velocities. Figures 6(*a*) and (*b*) show the transport velocities of turbulent energy in the y and z directions defined as

$$V_q = \frac{\overline{u^2v} + \overline{v^3} + \overline{vw^2}}{\overline{u^2} + \overline{v^2} + \overline{w^2}}, \tag{1}$$

$$W_q = \frac{\overline{u^2w} + \overline{v^2w} + \overline{w^3}}{\overline{u^2} + \overline{v^2} + \overline{w^2}} \tag{2}$$

respectively. These definitions omit diffusion by pressure fluctuations, for which we offer: (i) the argument that this contribution is negligible where it can be checked

by difference, e.g. in the outermost part of a two-dimensional boundary layer; and (ii) the excuse that pressure fluctuations within the flow cannot be measured with any assurance of accuracy. Both transport-velocity distributions are rather complicated, but the main features are easily distinguished. V_q is positive everywhere, with a peak at about $z = -45$ mm, $y = 15$ mm, where the boundary layer is thinned by the negative V-component velocity induced by the vortex. In the region of positive $\partial\overline{q^2}/\partial y$ near $z = -25$ mm, $y = 20$–30 mm, V_q is smaller than elsewhere, but not negative as would be expected from gradient-diffusion arguments. W_q does change sign, roughly in accordance with the sign of $\partial\overline{q^2}/\partial z$, and the negative region at $z = +70$ mm is probably genuine, although it appears in only one traverse.

The v-component transport velocity of $\overline{uv}$, defined as $V_{uv} = \overline{uv^2}/\overline{uv}$ and shown in figure 6(*c*), has a strong negative region on the positive-z side of the vortex, and the maximum value reached near the edge of the shear layer is somewhat smaller above the vortex than elsewhere. This negative region in $\overline{uv^2}$ does not correspond to a negative gradient, or even any particular noticeable feature, of $\overline{uv}$ itself. It does, of course, coincide with the region in which fluid is transported away from the surface by the secondary flow, and may therefore be a natural response of inner-layer turbulence when convected away from the solid surface which previously prevented downward transport of $\overline{uv}$: this is not just a passive distortion of contours by the secondary flow, which would suffice to explain the corresponding protrusion in the contour $V_q/U_e = 0.005$ in the region of $y = 30$ mm, $z = -20$ mm (figure 6*a*). The z-wise transport velocity of $\overline{uw}$, $W_{uw} = \overline{uw^2}/\overline{uw}$, reaches quite large values on either side of the vortex; unexpectedly, the values on both sides are positive in the outer part of the boundary layer (indicating transport in the positive-z direction) and negative in the inner part of the boundary layer. We recall from figure 4(*e*) that $\overline{uw}$ itself is – very roughly – symmetrical about the vortex position (so that gradient diffusion would imply lateral transport away from the vortex core on either side): we also note that $\overline{uw}$ remains quite significant out to the lateral limits of measurement, although $\overline{uv}$, for instance, has asymptoted to two-dimensional values.

One of the main messages of this paper is summed up by the comparison between the transport velocities in figure 6 and the eddy diffusivities in figure 7. The complication of the contours of the eddy diffusivity of $\overline{uv}$, shown in figure 7(*a*), contrasts with the general simplicity of the contours of the transport velocity of $\overline{uv}$ shown in figure 6(*c*). Even the w-component transport velocity of $\overline{uw}$, complicated though it is, varies less violently than the corresponding diffusivity. Physically, the concept of a transport velocity is more plausible than that of eddy diffusivity if one believes that turbulent transport is effected by the large eddies, rather than by eddies with a mean free path small compared to the dimensions of the flow. However, the justification for preferring transport velocities to describe turbulent transport of Reynolds stresses in a flow with numerous extrema of stress gradient is purely pragmatic: eddy diffusivities of Reynolds stress go to infinity at extrema of the Reynolds stresses, while transport velocities go to infinity only at zeros of the Reynolds stresses, which are usually less frequent.

5. Conclusions

The measurements presented here can be regarded as a sequel to those of Shabaka & Bradshaw (1981) on a longitudinal vortex generated at the leading edge of, and constrained by, a wing–body junction. The present flow, although artificially generated, is more general, representing the many cases in which a longitudinal vortex

appears on a nearly flat surface. The data are intended as input to, or as a test case for, calculation methods. We do not pretend to understand the details of the processes involved in the interaction between a vortex and the boundary layer – 'understanding' a fluid flow amounts to mental integration of an adequate approximation to the relevant equations of motion, which is hardly possible in the present case where the equations are almost fully general. Therefore the following conclusions are purely qualitative.

The mean-velocity and Reynolds-stress contours are generally what would be expected from the superposition of the secondary-flow velocity pattern of a vortex on a pre-existing turbulent boundary layer, and from the general principle that fluxes of momentum will normally be down the momentum gradient. However, the detailed patterns show some interesting features, notably the region of very small, or slightly negative, shear stress near the 'downgoing' side of the vortex. The vorticity contours show that vorticity of opposite sign to that in the main vortex is generated in regions around the main vortex, as would be expected if a vortex were suddenly introduced into fluid which had negligible vorticity in the direction of the vortex. (The aircraft trailing vortex, with non-zero circulation outside the vortex, is a very special case.) Some vorticity of opposite sign also resides in the boundary layer itself, as the result of cross flow induced by the vortex: this secondary vorticity was found by Harvey & Perry (1971) and is an accepted feature of slender-wing vortices.

Structural changes in the turbulence are demonstrated by the large variations of shear correlation coefficient and stress–energy ratio, both nearly universal constants in conventional boundary layers. Correlation coefficients for the shear stresses $\overline{uw}$ and $\overline{vw}$ achieved numerical values not far short of the primary shear-stress correlation coefficient R_{uv}, indicating a strong organization of the secondary Reynolds shear stresses.

The behaviour of the triple products, of which only a few examples are given in the present paper, is extremely complicated, but contours of the Reynolds-stress transport velocities (defined as a triple product divided by the Reynolds stress that it diffuses) have a much smoother pattern than contours of the eddy diffusivities of Reynolds stress, which go to infinity at points where stress gradients become zero.

The work on which all three parts of this paper are based was supported by the U.S. Office of Naval Research, contract No. N 00014-78-G-0032, Task NR 061-256, monitored by Mr Morton Cooper. We are grateful to Professor B. R. Morton for helpful comments on vortex behaviour, and to Miss S. Mokhtari for performing some check measurements.

REFERENCES

BRADSHAW, P. 1972 Two more low-turbulence wind tunnels driven by centrifugal blowers. *Imperial College Aero Rep.* 72-10.

BRADSHAW, P. 1975 Review – Complex turbulent flow. *Trans. ASME* I: *J. Fluids Engng* **97**, 146.

BRADSHAW, P., SHABAKA, I. M. M. A. & MEHTA, R. D. 1982 Turbulent vortex flows, final report on ONR contract N 00014-78-G-0032. *Imperial College Aero Tech. Note* 82-103 (available on microfiche): AD-A124 063/9.

HAINES, D. A. & SMITH, M. C. 1983 Wind tunnel generation of horizontal roll vortices over a differentially heated surface. *Nature* **306**, 351.

HARVEY, J. K. & PERRY, F. J. 1971 Flow field produced by trailing vortices in the vicinity of the ground. *AIAA J.* **9**, 1659.

HOFFMANN, H. P. 1976 Untersuchung der 3-dimensionalen turbulenten Grenzschicht an einem Schiffsdoppelmodell im Windkanal. *Inst. für Schiffbau, Universität Hamburg, Ber.* 343.

HOFFMANN, P. H., MUCK, K. C. & BRADSHAW, P. 1984 The effect of concave surface curvature on turbulent boundary layers, submitted to *J. Fluid Mech.*

HUMPHREY, J. A. C., WHITELAW, J. H. & YEE, G. 1981 Turbulent flow in a square duct with strong curvature. *J. Fluid Mech.* **103**, 443.

KLINE, S. J., CANTWELL, B. J. & LILLEY, G. M. (eds.) 1981 *Proc. 1980–81 AFOSR-HTTM-Stanford Conf. on Complex Turbulent Flows*, vol. 1.

KLINE, S. J., CANTWELL, B. J. & LILLEY, G. M. (eds.) 1982 *Proc. 1980–81 AFOSR-HTTM-Stanford Conf. on Complex Turbulent Flows*, vol. 2.

LARSSON, L. (ed.) 1981 *SSPA-ITTC Workshop on Ship Boundary Layers 1980. SSPA, Gothenburg, Pub.* 90.

MOKHTARI, S. & BRADSHAW, P. 1983 Longitudinal vortices in wind tunnel wall boundary layers. *Aero. J.* **87**, 233.

PEAKE, D. J. & TOBAK, M. 1980 Three-dimensional interactions and vortical flow with emphasis on high speeds. *AGARDograph* 252.

SHABAKA, I. M. M. A. & BRADSHAW, P. 1981 Turbulent flow measurements in an idealized wing/body junction. *AIAA J.* **19**, 131.

SMITS, A. J., YOUNG, S. T. B. & BRADSHAW, P. 1979 The effect of short regions of high surface curvature on turbulent boundary layers. *J. Fluid Mech.* **94**, 209.

TANAKA, I. & SUZUKI, T. 1978 Interaction between the boundary layer and longitudinal vortices. In *Proc. Intl Symp. on Ship Resistance, Gothenburg* (ed. L. Larsson).

WIEGHARDT, K. 1983 Kinematics of a wake flow. *Z. Flugwiss. Weltraumforsch.* **7**, 149.

YOUNG, A. D. 1977 Some special boundary layer problems. *Z. Flugwiss. Weltraumforsch.* **1**, 401.